ADVANCED FUNCTIONAL MATERIALS
www.afm-journal.de

Gold-Cobalt Nanoparticle Alloys Exhibiting Tunable Compositions, Near-Infrared Emission, and High T_2 Relaxivity

*Lauren E. Marbella, Christopher M. Andolina, Ashley M. Smith, Michael J. Hartmann, Andrew C. Dewar, Kathryn A. Johnston, Owen H. Daly, and Jill E. Millstone**

We demonstrate the synthesis of discrete, composition-tunable gold-cobalt nanoparticle alloys (% Co = 0–100%; diameter = 2–3 nm), in contrast with bulk behavior, which shows immiscibility of Au and Co at room temperature across all composition space. These particles are characterized by transmission electron microscopy and ^{1}H NMR techniques, as well as inductively coupled plasma mass spectrometry, X-ray photoelectron spectroscopy, and photoluminescence spectroscopy. In particular, ^{1}H NMR methods allow the simultaneous evaluation of composition-tunable magnetic properties as well as molecular characterization of the colloid, including ligand environment and hydrodynamic diameter. These experiments also demonstrate a route to optimize bimodal imaging modalities, where we identify Au_xCo_yNP compositions that exhibit both bright NIR emission (2884 $M^{-1}cm^{-1}$) as well as some of the highest per-particle T_2 relaxivities (12200 $m_{M_{NP}}^{-1}s^{-1}$) reported to date for this particle size range.

1. Introduction

The now canonical relationship between nanoparticle morphology and nanoparticle physical properties is remarkable and continues to produce an inspiring suite of new materials,[1] physical insights,[2] and technological capabilities.[3] In the case of metallic nanoparticles, the majority of these advances have been made with particles comprised of a single element.[1b–e,2d–f,3a–c,e] Yet, centuries of metallurgy indicate that a vast new dimension of particle properties and applications may emerge with the creation of alloyed nanoparticle colloids.[4] Further, in applications with narrow tolerance for particle dimensions and/or surface chemistry (e.g., biologic or catalytic applications)[5] accessing a diversity of nanoparticle behaviors from a single composition is challenging. To address this challenge, a variety of multimetallic nanoparticles have been synthesized including core-shell, hollow, Janus, and alloyed morphologies.[6]

L. E. Marbella, Dr. C. M. Andolina, A. M. Smith, M. J. Hartmann, A. C. Dewar, K. A. Johnston, O. H. Daly, Prof. J. E. Millstone
Department of Chemistry
University of Pittsburgh
Pittsburgh, Pennsylvania 15260, USA
E-mail: jem210@pitt.edu

DOI: 10.1002/adfm.201400988

One attractive class of alloys is the combination of noble metals with more earth-abundant transition metals. These metal mixtures have generated considerable interest for cost reduction and/or performance enhancement of precious metal catalysts[7] as well as for stabilization (e.g., from oxidation) of ferromagnetic elements such as Fe and Co in materials for data storage[8] and theranostic applications.[9] Optical properties can also be enhanced via alloying.[10] For example, we have reported the composition-tunable near-infrared (NIR) photoluminescence (PL) properties of gold-copper (Au_xCu_y) nanoparticle alloys (diameter, d = 2–3 nm).[11] Combining the optical features of Au with ferromagnetic (in the bulk) elements such as Ni, Co, or Fe is an opportunity to leverage several of these effects within a single particle architecture.

However, bulk phase diagrams indicate that Au is largely immiscible with each of these metals at temperatures below 400 °C.[12] In the case of cobalt, the immiscible behavior is dramatic, with no miscibility or intermetallic states predicted below 400 °C across all composition space.[12b] Likewise, simulations for surface alloys of Au and Co consistently predict segregation behavior for both Au host-Co solute and Co host-Au solute surfaces.[13] Yet, some reports indicate that materials at the nanometer length scale may deviate significantly from these trends. At particle sizes between 95–2590 atoms, Nørskov and co-workers have reported that particle size alone can influence metal segregation behaviors.[14] More recently, Schaak and co-workers have developed a spectrum of preparations for the formation of nanocrystalline alloyed materials, which are analyzed to be representative of $L1_2$ intermetallic states.[15] In particular, the authors use metal diffusion at 250 °C to create Au_3Ni, Au_3Fe, and Au_3Co particles with dimensions ranging from ~10–30 nm. Interestingly, these intermetallics are not predicted by bulk phase diagrams, and instead were one of the first indications that nanoscale colloids may form a greater diversity of alloyed architectures than has previously been observed in the bulk.

Here, we use a combination of rapid metal ion reduction and surface chemistry-based strategies to form small (d = 2–3 nm), discrete, composition-tunable gold-cobalt nanoparticle

Table 1. Size, composition, photoluminescence, and magnetic property analysis of Au_xCo_yNPs.

Initial molar ratio added [% Co]	NP composition [% Co] ICP-MS	Lattice constant [Å] HRTEM	NP size [nm] HRTEM	NP size [nm] PFGSE-NMR	ε at 360 nm [$\times 10^5 M^{-1}cm^{-1}$]	Φ [$\times 10^{-3}$]	Brightness [$M^{-1}cm^{-1}$]	Magnetic susceptibility $\times$ [10^{-6} $cm^3 g_{NPs}^{-1}$]	r_2 [$m_{M_{Co}}^{-1}s^{-1}$/ $m_{M_{NP}}^{-1}s^{-1}$] 7 T
0	0 ± 0	3.96 ± 0.05	2.2 ± 0.5	4.1 ± 0.1	9.3 ± 2.3	0.40 ± 0.02	374	–0.65 ± 0	NA
50	1.6 ± 0.1	3.85 ± 0.03	2.3 ± 0.5	4.2 ± 0.1	12.6 ± 4.8	2.29 ± 0.49	2884	–0.39 ± 0.04	NA
60	7.7 ± 0.7	3.70 ± 0.03	2.2 ± 0.2	4.3 ± 0.3	8.7 ± 1.2	2.80 ± 0.64	2430	–0.20 ± 0.05	1.5/49
70	26.8 ± 2.0	3.75 ± 0.04	2.3 ± 0.5	4.3 ± 0.1	4.6 ± 1.1	3.00 ± 0.15	1373	0.55 ± 0.34	2.4/209
80	48.1 ± 2.7	3.73 ± 0.03	2.2 ± 0.3	4.1 ± 0.3	9.2 ± 1.8	2.52 ± 0.36	2322	3.24 ± 0.96	6.8/1750
85	62.0 ± 2.0	3.88 ± 0.05	2.1 ± 0.2	4.3 ± 0.4	6.1 ± 0.9	0.50 ± 0.26	305	5.34 ± 1.01	11/3650
90	80.7 ± 2.5	3.90 ± 0.05	2.2 ± 0.4	4.3 ± 0.1	7.1 ± 0.1	0.30 ± 0.16	211	8.51 ± 1.23	NA
100	100 ± 0	4.79 ± 0.05	2.9 ± 0.5	4.9 ± 0.1	NA	NA	NA	11.26 ± 1.34	26/12200

*All reported values are the average of at least 3 independently synthesized trials. The values for NP size (TEM) are reported with the standard deviation of the measurement for N > 100 nanoparticles. All other values are reported with the standard error.

(Au_xCo_yNP) alloys at room temperature in water. This approach produces Au_xCo_yNPs across a wide range of compositions (0 to 100% Co) and indicates a new pathway to synthesize these previously inaccessible alloys. The resulting particles exhibit composition-tunable magnetic susceptibility as well as some of the highest reported values for T_2 relaxivity as compared to superparamagnetic iron oxide nanoparticles (SPIONs) in a similar size range.[16] At the same time, the particles retain attractive optical features associated with Au at this length scale, specifically, bright NIR emission. Tuning composition, we then identify optimum architectures for bimodal imaging properties, while maintaining particle size and surface chemistry.

2. Results and Discussion

In a typical experiment, Au_xCo_yNP alloys were synthesized by co-reduction of $HAuCl_4$ and $Co(NO_3)_2$ with $NaBH_4$ at room temperature in an aqueous solution containing the capping ligand, poly(ethylene glycol) methyl ether thiol (PEGSH, average M_n = 1000 Da). $NaBH_4$ is an attractive reducing agent because it is water soluble, can reduce both metal precursors,[17] and in pure metal nanoparticle syntheses (e.g. Au and Ag), the oxidized byproducts are not known to influence the reaction. We choose a thiolated ligand, because they are associated with the synthesis of small, stable Au nanoparticles.[17a] A PEG moiety is chosen for water solubility and biocompatibility. The initial molar ratio of Co to Au was varied from 0–100% Co, while maintaining the same total metal, capping ligand, and reducing agent concentrations (complete synthesis details are included in Experimental and Supporting Information (SI) sections). All nanoparticle products were characterized using UV–visible spectroscopy, inductively coupled plasma mass spectrometry (ICP-MS), X-ray photoelectron spectroscopy (XPS), photoluminescence spectroscopy, transmission electron microscopy (TEM), and ^{1}H nuclear magnetic resonance (NMR) techniques. Figures of merit from these studies are listed in **Table 1**. **Figure 1** shows high-resolution transmission electron microscopy (HRTEM) images of Au_xCo_yNPs (x = 100% – y; y = 26.8 ± 2.0% Co as measured by ICP-MS; see Figure S2 for HRTEM of additional Au_xCo_yNP compositions). In all cases, Au_xCo_yNPs are observed as pseudospherical, discrete, and crystalline nanoparticles with average metallic core diameters between 2.1–2.3 nm and a standard deviation of <20% (Figure 1 and Figure S2). The hydrodynamic diameter of the Au_xCo_yNPs was calculated from the diffusion coefficient as measured by pulsed-field gradient stimulated echo (PFGSE) ^{1}H NMR. The hydrodynamic diameters of all Au_xCo_yNPs are 4.1–4.3 nm, consistent with a 2.1–2.3 nm metallic core diameter capped with a monolayer of random coil PEGSH (M_n = 1000 Da).

To assign the composition and composition morphology of the resulting particles, we use a combination of several techniques. First, we analyze particle crystallographic features using HRTEM. The bulk lattice constant of Au_{fcc}, a = 4.079 Å and the

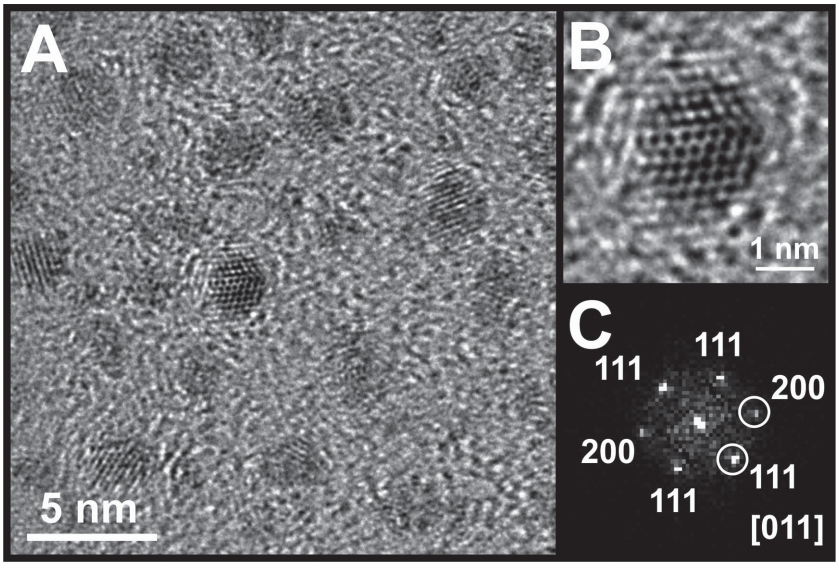

Figure 1. A) HRTEM image of Au_xCo_yNPs (y = 26.8 ± 2.0%). B) Magnified image of an individual Au_xCo_yNP and C) the corresponding FFT.

bulk lattice constant of metallic Co_{hcp}, a = 2.503 Å, c = 4.061 Å or Co_{fcc}, a = 3.545 Å.[18] Therefore, regardless of the overall crystal system adopted by the particle, as % Co increases, the particle lattice constant(s) are expected to decrease with respect to either bulk Au or the lattice constant of a pure Au particle of this size (100% AuNPs = 3.96 Å, Table 1). Initially, our results follow this trend where increasing Co incorporation leads to a decrease in observed particle lattice constants (Table 1). However, as the % Co incorporation reaches a threshold (>60%), the observed lattice constants begin to increase. This increase is likely due to the formation of a cobalt oxide, which may be expected since our synthesis is conducted in air and in water (this assignment is supported by XPS analysis, vide infra and Figure S6). Importantly, no core-shell architectures are observed in either HRTEM or scanning transmission electron microscopy (STEM) analysis (Figure S4), and the distribution of lattice constants is not bimodal, indicating that there are not two populations of particles each comprised of only one metal.

After analysis of lattice features and general morphology, we use three techniques to analyze elemental composition. ICP-MS and XPS were used to evaluate the metal atom concentrations and oxidation states of the bulk colloid, respectively. STEM-EDS point spectra were used to assess the composition of individual particles (Figures S4, S8 and Tables S2, S3). ICP-MS analysis indicates that little to no Co incorporation is observed until the initial molar ratio of Co was increased to 50%. At initial molar ratios above 50% Co, the nanoparticles exhibit a continuously tunable stoichiometry, and the final incorporation of Co into the Au nanoparticles was varied from 1.6 – 89.8% (Figure S8 and Table 1). The initial lag in Co incorporation may be a product of the disparity in reduction potential between Co(II) and Au(III) species[18] which results in less available Co monomer (here, referring to "monomer" as described by LaMer[19]) at the critical concentration for homogeneous nucleation of the particle solid phase. Previous reports indicate that co-reduction during nucleation was a crucial factor in the formation of intermetallics and larger alloyed shells.[15b,20] Differences in reduction potential are also thought to play a large role in the formation of core-shell particles or incomplete mixing of the two components (e.g., heterogeneous solid solution or "island" formation).[20b] We hypothesize that above 50% initial molar ratio of Co, a threshold amount of Co monomer is available to co-nucleate with Au monomer, allowing both elements to be incorporated into a single particle.

To analyze the composition of individual particles, we use STEM-EDS point spectra. For a sample of nanoparticles synthesized with a given molar ratio of Au:Co, individual particle compositions were measured by EDS, and spectra were obtained from several different particles to establish an average particle composition. Average compositions agreed well between ICP-MS and STEM-EDS analysis. However, it is important to note that using STEM-EDS, we observed that particle-to-particle composition was more heterogeneous as % Co increased, and this heterogeneity is consistent with the increased variation for the same initial molar ratios as measured by ICP-MS (i.e., the standard error for composition increases with increasing % Co, Table 1 and Figure S8). Particle-to-particle composition heterogeneity may be a result of our synthetic strategy. For example, the rapid particle nucleation approach can be viewed as an analog to the bulk diffusion-quench processes used to form bulk alloys. In diffusion-quench methods, a given ratio of two metals are heated together and entropy drives metal mixing. The mixture is then cooled to "freeze" the combined state.[4a] In our synthesis, instead of cooling, we rapidly increase the solution saturation in metal precursor, which induces nucleation of the solid phase. During this step, there may be limited selectivity for metal incorporation into the particle. Instead, we hypothesize that the local molar ratio of metal precursor in solution determines the ratio of the two metals incorporated into the final nanoparticle architecture. It is important to note that comparison of XRD spectra to determine particle composition was not possible from particles of this size range due to significant line broadening, which is consistent with mathematical predictions of X-ray optics (see SI).

To further characterize the composition and oxidation state of the Au_xCo_yNP alloys, all particle compositions were analyzed by XPS (Figures S5 and S6). Survey spectra showed the presence of Au, Co, C, O, and S in all samples (with the exception of Au_{100}NPs and Co_{100}NPs, which lacked Co and Au peaks, respectively). Previous syntheses using pure Co precursor under similar reaction conditions have also observed boron in the particle products,[21] however we do not observe boron signal in any XPS spectra (Figure S7), which indicates that borohydride, borate byproducts or cobalt-boride materials are not present in the purified final nanoparticle products. A shift of the $Au4f_{7/2}$ peak from Au_{100}NPs at 83.8 eV to higher energy is observed with increasing % Co incorporation, suggesting a continuous change in the Au environment that is consistent with alloy formation.[20,22] Analysis of the $Co2p_{3/2}$ peak shows the presence of metallic cobalt as a sharp, narrow band with binding energies ranging from 778.0–778.4 eV, in all cases. From a pure Co phase to an alloyed phase, we observe a shift to lower binding energy of the Co2p features. From a pure Au phase to an alloyed phase, we observe a shift to higher binding energy of the Au4f peaks. These binding energy shifts do not follow trends expected from electronegativity arguments, but instead are consistent with electron density moving from Au to Co. Similar trends have been observed for other Au-transition metal alloys, such as Au-Ni, where $Ni2p_{3/2}$ binding energies decrease and $Au4f_{7/2}$ binding energies increase when comparing the pure metal phase to an alloyed composition.[23] For high concentrations of Co (>60% Co incorporation) a shoulder is present at ≈781 eV. This binding energy region is consistent with Co(II) or Co(III) species. However, no corresponding satellite peaks are observed (≈786 eV), which indicates that where oxidation is present, the concentration is low (Figure S6). Limited oxidation of the Co, despite a synthesis conducted in air and water, is consistent with stabilizing trends observed in other noble-transition metal alloys such as PtFe[8] and PtCo,[24] where the first row transition metal exhibits enhanced resistance to oxidation when alloyed with a more noble counterpart.

Next, we analyze particle magnetic properties and also use this analysis as an additional metric to assess composition tunability. In order to determine the magnetism of Au_xCo_yNPs, we have used the Evans' method[25] to measure the mass magnetic susceptibility at room temperature. Here, the Evans' method is an alternative to superconducting quantum interference device (SQUID) analysis, which requires significantly more material,

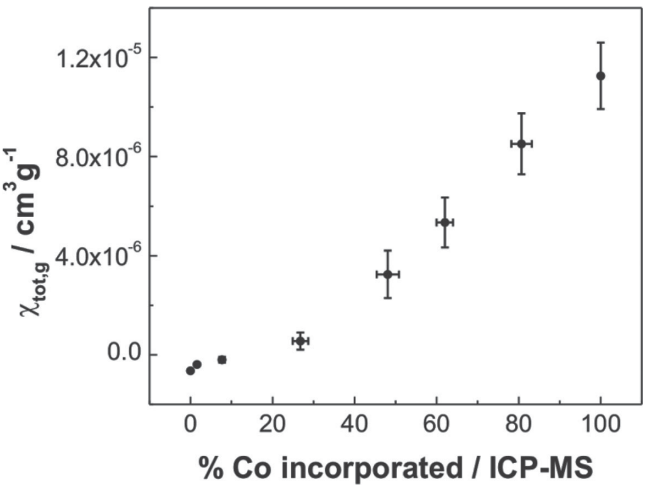

Figure 2. Magnetic susceptibility of Au_xCo_yNPs increases as % Co increases. Error bars in both χ and % Co incorporated represent the standard error of at least 6 independent experiments.

especially for small particle sizes where diamagnetic capping ligands can quench the magnetism of surface atoms,[26] which are a large percentage of total atoms in the sample (~40% for d = 2.2 nm). Using the Evans' approach, we analyzed a series of Au_xCo_yNP compositions (0–100% Co incorporation with 5% initial molar ratio step sizes, **Figure 2** and Figure S10), to determine the relationship between particle composition and particle susceptibility. Here, we found that by controlling the % Co incorporated in the final Au_xCo_yNPs we could achieve continuously tunable magnetic susceptibility from -0.39×10^{-6} to 11.26×10^{-6} $cm^3g_{NPs}{}^{-1}$. The reported values represent the total mass magnetic susceptibility of the sample, which is comprised of both the diamagnetic and paramagnetic contributions (Table 1). The magnetic susceptibility values reported here, as well as relaxivity measurements discussed below, are consistent with previous reports of a variety of superparamagnetic nanoparticles, including AuNi nanoparticles[27] and SPIONs.[16,28]

By using a molecular characterization method to analyze our magnetic susceptibility, we were also able to directly observe the ^{1}H NMR spectrum of the NP ligand shell in each sample within a single experiment (see SI; 1D ^{1}H NMR spectra in Figure S9). Here, ^{1}H NMR spectra show an absence of the thiol proton as well as the directly adjacent CH_2 protons on the PEGSH (Figure S11). The absence of these peaks from the ^{1}H NMR spectra is consistent with significant dephasing, which is expected to be a result of a chemical shift distribution from various PEGSH binding sites as well as conduction electrons at the NP surface. Control experiments were performed to ensure that changes in magnetic susceptibility and relaxivity were not the result of excess reactant impurities (see Figure S11 and corresponding discussion).

Remarkably, Au_xCo_yNPs also exhibit PL in the NIR spectral region, which to the best of our knowledge, is the first observation of PL from Au-Co alloys at any length scale. Here, all compositions of the Au_xCo_yNPs exhibit NIR PL, with the exception of 100% CoNPs (Table 1). Excitation spectra from these particles are consistent with previous excitation spectra obtained for Au and Au_xCu_yNPs[11] (Figure S19). Interestingly, in the case of Au_xCo_yNPs, a hypsochromic shift (≈25 nm) in the maximum emission wavelength relative to 100% AuNPs is observed (**Figure 3**) with increasing % Co incorporation. This trend is observed until Co concentration in the nanoparticle reaches >60% incorporation. Beyond this concentration, the maximum emission wavelength exhibits a bathochromic shift toward the emission maximum from 100% AuNPs. This % Co composition is also coincident with our observation of increases in Co oxidation via XPS, as well as increases in lattice constants.

Previous work indicates that the NIR emission originates from a surface charge-transfer state comprised of Au-thiolate interactions.[29] In the case of the Au_xCu_yNPs, we hypothesized that the presence of Cu in the surface region (surface or subsurface layers)[30] changes the energy of this Au-thiolate interaction possibly by replacing one or more of the bonding Au atoms with a Cu atom, consistent with previous reports.[31] The presence of PL from the Au_xCo_yNPs, but less dramatic composition dependence of the maximum λ_{EM} (Figure 3), indicates that the incorporation of Co into the NP either does not significantly alter the energy of the emissive luminophore (excited or ground states), or Co is not proximate to the luminophore. We can further delineate these scenarios as 1) only a small population of Co exists on the NP surface (where the emitting state has been indicated to localize), 2) Co is oxidized on the surface of the particle and therefore does not interact with the luminophore of the NP, 3) Co is segregated into Co "islands" on the surface, 4) Co does not alter the energy of the emissive state in contrast to Cu in Au_xCu_yNPs and/or 5) Co *does* alter the energy of the emissive state, but at high % Co compositions, compositional

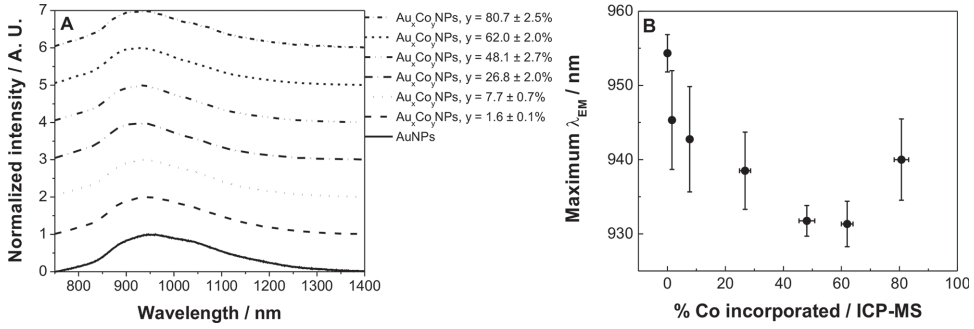

Figure 3. A) Photoluminescence of Au_xCo_yNPs in D_2O showing representative emission spectra. B) Maximum emission wavelength as a function of % Co incorporated.

heterogeneity and increasing oxidation confounds subsequent interpretation. Mechanism 4 is unlikely, given that all Au_xCo_yNPs exhibit an emission maximum that is blue-shifted from 100% AuNPs. HRTEM analysis indicates that the Au_xCo_yNPs do not exhibit large scale (i.e., observable) metal separation throughout the particle, which seems to eliminate mechanism 3. Based on our current experimental evidence, mechanisms 1 and 5 are the most probable explanations for the composition dependence of the maximum λ_{EM} from Au_xCo_yNPs.

Although the definitive mechanism of PL for these small Au-transition metal NPs is still being determined, standard PL characterization is possible. Quantum yield (Φ) and molar extinction coefficient (ε) measurements were used to calculate particle brightness ($\varepsilon \times \Phi$). The brightness value determines the probability of absorbed and emitted of photons and is a useful figure of merit to compare luminophores.[32] Measured quantum yield values are consistent with those found for other noble metal nanoparticle systems (Table 1). Quantum yield and brightness varied non-linearly (Table 1) as a function of composition (Figures S16A-S18A) with the brightest particles containing ≈2% Co.[11] Au_xCo_yNPs exhibit no observable size dependence of optical properties (Figure S15, S16B-18B). Nanoparticle PL was evaluated in both D_2O and H_2O. D_2O was used to eliminate solvent absorption interference, however evaluation in H_2O was also conducted in order to facilitate comparison with other luminophores that have been measured in non-deuterated solvents. All optoelectronic properties were the same, within error, in both solvents. For comparison, an emission spectrum of Au_xCo_yNPs ($y = 48.1 \pm 2.7\%$) in H_2O is shown in Figure S14. The Au_xCo_yNPs display brightness values that are over an order of magnitude higher than alternative biocompatible probes such as (Yb(III)TsoxMe), a sensitized lanthanide complex evaluated in water (2884 $M^{-1}cm^{-1}$ vs 83 $M^{-1}cm^{-1}$).[33]

The combination of magnetic and optical properties from Au_xCo_yNPs are clearly interesting for application as multimodal MRI contrast agents and therefore the relaxivity properties of each particle composition were also evaluated. Previous reports indicate that metallic Co T_2 relaxivities are both field-strength and concentration dependent.[34] To study the effect of field strength, the relaxivity of the Au_xCo_yNPs was measured at 37 °C at two different static fields, 0.47 T (20 MHz proton Larmor frequency) and 7 T (300 MHz proton Larmor frequency) (Table S4). As a control experiment, the relaxivity of 100% AuNPs was measured, and no effect on relaxivity was observed. For both field strengths, Au_xCo_yNPs had a significant effect on the transverse relaxation time (T_2) of water, and had little to no influence on the longitudinal relaxation time (T_1). These results indicate that Au_xCo_yNPs have the ability to maintain proton T_1 values that are the same as the surrounding tissue (providing essentially no positive contrast properties) while significantly dephasing the transverse magnetization used in MRI signal detection.[35] This property most efficiently produces negative (dark) spots in the final image, making Au_xCo_yNPs attractive negative-T_2 contrast agents.

Even at low field strength, all Au_xCo_yNP compositions show very little effect on T_1, leading to r_2/r_1 values that, in all cases, are either comparable to or larger than those of a clinically available T_2 contrast agent, Ferumoxsil (SPION), which has a diameter nearly 3 times larger than the Au_xCo_yNP alloys reported here.[28b] The comparable or in some cases, enhanced, relaxivity for Au_xCo_yNPs (despite their smaller diameter compared to reported SPIONs) is likely the result of the higher saturation magnetization of Co compared to iron oxide (see SI for a full comparison of Au_xCo_yNPs to previously reported iron oxide nanoparticles).[18] Since tissues already have relatively short T_2 times (~10^2–10^3 ms),[36] in order to be considered an effective negative T_2 contrast agent, r_2 values must be orders of magnitude larger than r_1 values typically required for positive contrast agents. Further, as field strength is increased, T_1 effects, as well as the efficiency of positive contrast agents, are expected to diminish. As clinical imaging instrumentation moves to higher field strengths to achieve greater resolution, the necessity to develop and implement improved contrast agents for T_2 weighted imaging becomes increasingly important.[37]

Au_xCo_yNP alloys may provide a platform to achieve T_2 enhancements greater than those observed from SPIONs, while maintaining a small particle size for renal clearance.[5a] As expected, at 7 T longitudinal relaxation times in the presence of even the most concentrated Au_xCo_yNPs is equal to that of pure water (~6 s at 7 T). Both the per-Co and per-particle T_2 relaxivities at 7 T are listed in Table 1. Relaxivity values are reported as per-particle relaxivity values, in addition to per-Co relaxivity values, to facilitate comparison between nanoparticles of different composition and size.[34] The per-particle comparison is made here due to the difference between superparamagnetic nanoparticles and chelated-metal based contrast agents. For chelated-metal contrast agents, such as commercially available gadolinium-based agents, water protons bind to a single metal center, and therefore per-metal relaxivities are preferred. For superparamagnetic nanoparticles, the particle itself behaves as a large paramagnetic ion.[38] Therefore, per-particle relaxivities provide a more accurate assessment of contrast agent efficiency in the case of nanoparticles[34] (but with the caveat that larger particles will almost always exhibit higher relaxivities compared with smaller particles of the same material, and this relationship between particle size and per-particle relaxivity is not necessarily linear depending on the particle system).[38] To compare Au_xCo_yNP T_2 relaxivities to other contrast agents, the per-particle relaxivity was calculated for reported earth-abundant metal nanoparticles of comparable size. Indeed, Au_xCo_yNPs exhibit comparable or enhanced per-particle T_2 relaxivities compared to SPIONs, despite the fact that Au_xCo_yNPs are smaller in diameter. Additionally, Au_xCo_yNPs show improved T_2 relaxivities compared to 0D and 1D gold-cobalt ferrite and gold-iron oxide heterostructures.[39] Most relaxivities in the literature are reported as per-metal relaxivities. This figure of merit is important, as biological compatibility and toxicity is likely to be a function of transition metal concentration (for cobalt as well as iron), allowing a more straightforward assessment than particle concentration (although both cobalt and iron are used already in biomedical applications such as surgical implants).[40]

Because a wide range of Au_xCo_yNP compositions can be accessed via the current synthesis, the % Co incorporation parameter was explored to find a composition with both high NIR brightness and high T_2-relaxivity. This optimal composition can be determined by plotting r_2 at 7 T and NIR brightness as a function of % Co incorporation (**Figure 4**). Particle

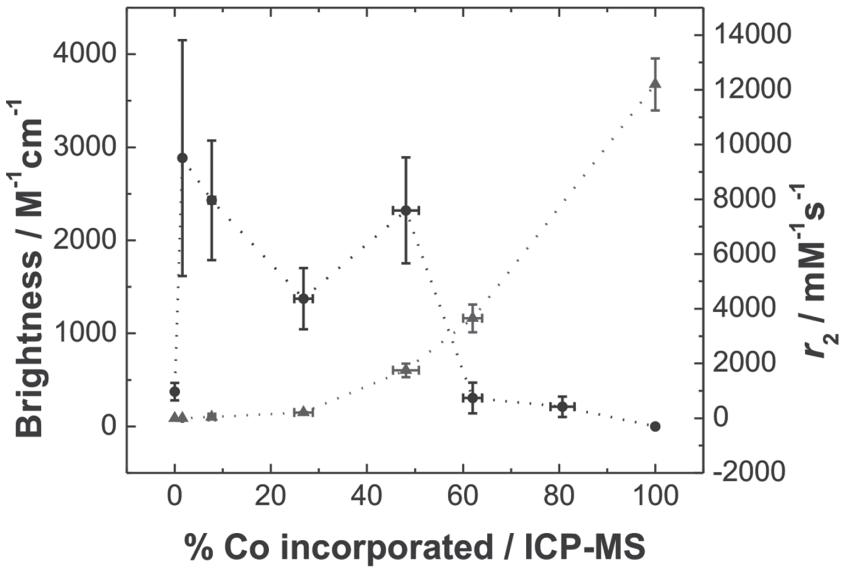

Figure 4. Optimal Au_xCo_yNP composition for bimodal NIR-T_2 contrast imaging occurs at y = 48.1 ± 2.7% Co incorporation.

brightness is highest for Au_xCo_yNPs (y = 1.6 ± 0.1%) and decreases until no NIR PL is observed. For per-particle relaxivity, as % Co incorporated increases, r_2 values become more favorable for negative MRI contrast. The trends for NIR brightness and r_2 intersect at approximately 55% Co incorporated in the particle. The particle composition closest to this value that retained desirable imaging properties was Au_xCo_yNPs, y = 48.1 ± 2.7%. Even at 48.1 ± 2.7% Co incorporation, the per-particle relaxivity (r_2 = 1750 $mM^{-1}s^{-1}$) remains competitive compared to marketed negative contrast agents[28b] and exceeds the relaxivity values for reported iron oxide nanoparticles of similar sizes.[16] Likewise, particle brightness (2322 $M^{-1}cm^{-1}$) also remains high when compared to other biocompatible NIR probes.[41] For this reason, we conclude that 48.1 ± 2.7% Co incorporation is an appropriate composition for a dual NIR-T_2 contrast imaging agent.

3. Conclusion

In summary, we present a method for preparing a previously inaccessible library of composition tunable Au_xCo_yNP alloys. This method can be used to tailor magnetic susceptibility while maintaining almost identical particle size and surface chemistry. To the best of our knowledge, these particles have also enabled the first observation of photoluminescence from a Au-Co nanoparticle species at any size range or composition. Combined, these magnetic and optical features generate a promising multi-modal agent that exhibits NIR emission and MRI contrast properties that meet or exceed current standards, all at small particle diameters. Taken together, these data suggest that alloying behavior at the nanoscale may deviate significantly from bulk trends and that access to these new stoichiometries should yield an exciting diversity of unique, tunable physical properties useful in applications ranging from multimodal theranostics to heterogeneous catalysis.

4. Experimental Section

4.1. Synthesis

Materials: Hydrogen tetrachloroaurate(III) trihydrate ($HAuCl_4{\cdot}3H_2O$, 99.999%), cobalt(II) nitrate hexahydrate ($Co(NO_3)_2{\cdot}6H_2O$, >99.99%), sodium borohydride ($NaBH_4$, 99.99%), dimethyl sulfoxide (DMSO, > 99.9%), were obtained from Sigma-Aldrich and used as received. Poly(ethylene glycol) methyl ether thiol (average M_n = 1000 Da) was obtained from Laysan Bio, Inc. or Sigma Aldrich (see SI for discussion of heterogeneity in commercially available PEGSH) and used as received. Deuterium oxide (D_2O) and DMSO-d_6 were purchased from Cambridge Isotope Laboratories, Inc. and used as received. NANOpure (Thermo Scientific, >18.2 MΩ cm) water was used to prepare all solutions unless otherwise indicated. Before use, all glassware and Teflon coated stir bars were washed with aqua regia (3:1 ratio of concentrated HCl and HNO_3 by volume) and rinsed thoroughly with water. Caution: Aqua regia is highly toxic and corrosive and requires proper personal protective equipment. Aqua regia should be handled in a fume hood only.

Synthesis of Au_xCo_yNPs: Au_xCo_yNP alloys were synthesized by co-reduction of $HAuCl_4$ and $Co(NO_3)_2$ with $NaBH_4$ at room temperature in an aqueous solution containing the capping ligand, poly(ethylene glycol) methyl ether thiol (PEGSH, average M_n = 1000 Da). Reagents were added to a glass vial, while stirring, in the following order: water (4.29 mL), $HAuCl_4$ (X mL, 20.0 mM), $Co(NO_3)_2$ (X mL, 20.0 mM), PEGSH (375 µL of 10.0 mM), and $NaBH_4$ (450 µL of 20.0 mM) (*N. B.* volume of metal stock added for each composition is listed in Table S1). The total concentration of metal cations was held constant while the molar ratio of Au and Co was varied. The initial molar ratio of Co to Au was varied from 0–100%, while maintaining the same total metal, capping ligand, and reducing agent concentrations.

Nanoparticle Purification: The entire contents of the NP synthesis were transferred to Amicon Ultra – 4 Ultracel 10 kDa molecular weight cutoff centrifugal filters (Merck Millipore Ltd.). Samples were purified from excess PEGSH and metal salts using an Eppendorf 5804 or 5804R centrifuge with swing bucket rotor (A-44–4) (Eppendorf, Inc.) with a force of 4000 RFC at 20 °C for 12–15 min. The resulting concentrated particles (typically ≈50 µL in water) were diluted in the concentrator tube to a volume of 3 mL with water. The loose pellet was resuspended by gentle mixing using a pipette prior to re-centrifugation. This washing procedure was repeated 5 times. Purified Au_xCo_yNPs were then characterized by electron microscopy techniques, UV–Visible spectroscopy, ICP-MS, XPS, photoluminescence, and ^1H NMR techniques.

4.2. Characterization

Electron Microscopy: Samples were prepared for electron microscopy by drop casting an aliquot of purified NP solution (diluted 1:10 or 1:100 with water) onto ultra-thin (3–5 nm) carbon type A 400 mesh copper grids (Ted Pella, Inc.). Samples were allowed to slowly air dry for at least 10 hours followed by drying under vacuum. Bright field, HRTEM and STEM characterization was performed using a JEOL JEM-2100F equipped with a Gatan GIF-Tridiem camera and Oxford Inca EDS detector operating at 200 kV (NanoScale Fabrication and Characterization Facility, Petersen Institute of NanoScience and Engineering, Pittsburgh, PA).

Size determination by NMR: Pulsed field gradient stimulated echo (PFGSE) ^{1}H NMR measurements were performed on a Bruker 500 Ultrashield magnet with an AVANCE III 500 Console or a Bruker 600 Ultrashield magnet with an AVANCE III 600 Console (Bruker Biospin, Billerica, MA) at 298 K. Au_xCo_yNPs NMR samples were lyophilized, resuspended in DMSO-d_6, and loaded in a 5 mm NMR tube for measurement. ^{1}H NMR diffusion spectra were acquired on a broadband observe probe using a stimulated echo bipolar pulsed field gradient pulse sequence (for calculations and additional analysis, see SI).

XPS Analysis: XPS was performed using a Thermo Scientific K-Alpha with monochromatic Al Kα X-rays (RJ Lee Group, Inc., Monroeville, PA). Survey and high resolution spectra were collected with a pass energy of 200 eV and 50 eV, respectively. Lyophilized NPs were resuspended in absolute ethanol and drop cast onto silicon wafers (University Wafer, Boston, MA). Prior to XPS collection, samples were sputtered for 30 seconds with an argon ion gun. All XPS spectra were measured with a 400 µm X-ray spot size. High resolution XPS spectra were charge referenced to the adventitious hydrocarbon C1s peak at 284.8 eV.

ICP-MS Analysis: ICP-MS analysis was performed using an Argon flow with a Nexion spectrometer (PerkinElmer, Inc.). An ultrapure aqua regia solution was prepared with a 3:1 ratio of hydrochloric acid (Sigma Aldrich > 99.999% trace metal basis): nitric acid (Sigma Aldrich, > 99.999% trace metal basis), a portion of which was diluted with NANOpure water for a 5% v/v aqua regia matrix. An aliquot of the purified nanoparticle samples was digested with ≈100 µL of ultrapure, concentrated aqua regia in a 10 mL volumetric flask, and diluted to volume with the 5% aqua regia solution. The unknown Au and Co concentrations were determined by comparison to a 5-point standard calibration curve with a range of 1–30 ppb prepared from a gold standard for ICP (Fluka, TraceCERT 1001 ± 2 mg/L Au in HCl) and a cobalt standard for ICP (Fluka, TraceCERT 1000 ± 2 mg/L Co in HNO_3), respectively, and diluted in the 5% aqua regia matrix. The ICP standards were measured 5 times and averaged, while all unknown samples were measured in triplicate and averaged. An 8 minute flush time with 5% aqua regia matrix was used between all runs, and a blank was run before every unknown sample to confirm removal of all residual metals.

Magnetic Susceptibility Measurements: Mass magnetic susceptibility for NPs were recorded on a Bruker 600 Ultrashield magnet (14.1 T) with an AVANCE III 600 Console or a Bruker 700 Ultrashield magnet (16.4 T) with an AVANCE III 700 Console (Bruker Biospin, Billerica, MA) equipped with a BVT3000 and BCU05 variable temperature unit, respectively. ^{1}H NMR spectra were collected at 298 K using the Evans' method.[25] Au_xCo_yNPs were synthesized and purified and the concentrated NP pellet was lyophilized. The mass of the dried NPs was recorded and resuspended in 1 mL of D_2O and loaded into a 5 mm NMR tube along with an internal sealed capillary tube of pure D_2O. A 1D ^{1}H NMR spectrum of each sample was recorded with 16 transients. ^{1}H NMR chemical shifts were referenced to the HDO peak from the capillary at 4.7 ppm. Typical 90° radiofrequency pulses were ~9 µs for ^{1}H NMR spectra, and were processed using Bruker Topspin 3.0 and iNMR. The distance in Hz between the residual HDO peak of the pure D_2O and the HDO peak of the D_2O containing the Au_xCo_y colloidal suspension (experimental ^{1}H NMR spectra shown in Figure S9) was measured and used to calculate the magnetic susceptibility (see SI for additional calculation details).

UV–Visible Spectroscopy: Molar Extinction Coefficient: Nanoparticle extinction coefficients were calculated using the UV–vis–NIR spectrum of the NPs after purification. Spectra were taken using a Cary 5000 UV–vis–NIR (Agilent, Inc.). UV–vis measurements were collected of nanoparticle suspensions diluted in D_2O using 1.0 cm quartz cuvettes (Hellma, Inc.).

Photoluminescence: Quantum Yield and Brightness: NP suspensions in D_2O were prepared from the purified Au_xCo_yNP stocks at concentrations ≤ 0.25 abs at 340 nm determined by UV–Vis. Emission spectra were acquired on a HORIBA Jobin Yvon IBH FluoroLog-322 spectrofluorometer equipped with a Hamamatsu R928 detector for the visible domain; DSS-IGA020L (Electro-Optical Systems, Inc.) detector for the NIR domain and a temperature controller using 1.0 cm × 0.4 cm quartz cuvettes (Hellma, Inc). A 780 nm NIR cut-on filter (Newport FSQ-RG780, Newport Corporation, Inc.) was used to block the excitation source. The quantum yields in the NIR region were determined by the optically dilute method. Excitation spectra of the purified Au_xCo_yNPs were collected using an emission slit of 20 nm centered at 950 nm with an excitation slit of 5 nm. Spectra were collected in 1 nm increments using an integration time of 0.4 s from 290–600 nm and the NIR cut-on (780 nm) filter was used to filter the emission (Figure S19). Excitation spectra have been corrected for lamp power fluctuations and the instrument response (see SI full calculations, spectra and analysis).

Relaxivity Measurements: Longitudinal (T_1) and transverse (T_2) relaxation time measurements were collected for five dilutions of each sample at 37 °C using an inversion recovery pulse sequence and the Carr-Purcell-Meiboom-Gill (CPMG) spin echo pulse sequence, respectively. Relaxation measurements were collected at both 20 MHz (0.47 T) on a Bruker mq20 minispec NMR analyzer and 300 MHz (7 T) on a Bruker DRX 300 MHz magnet. In order to minimize radiation damping effects at 7 T, the NPs were suspended in 50/50 H_2O/D_2O and the probe was de-tuned prior to measurement. All relaxivity measurements were performed in triplicate (three independent syntheses of each composition), with ICP-MS analysis of each sample for exact metal concentration (see SI for full calculations and comparison of alloys to other T_2 contrast agents).

Supporting Information

Supporting Information is available from the Wiley Online Library or from the author.

Acknowledgements

This work was supported by the National Science Foundation (CHE – 1253143) and the University of Pittsburgh. We thank Prof. Daniel J. Bain at the University of Pittsburgh for the use of his ICP-MS facilities. We also thank Dr. T. Kevin Hitchens and Dr. N. Thomas Nuhfer at Carnegie Mellon University for helpful discussions as well as use of the Bruker mq20 Minispec NMR Analyzer and electron microscopy facilities, respectively. We also thank Prof. Stéphane Petoud for use of his fluorometer and related materials.

Received: March 27, 2014
Revised: June 5, 2014
Published online: August 22, 2014

[1] a) R. Buonsanti, D. J. Milliron, *Chem. Mater.* **2013**, *25*, 1305–1317; b) M. Grzelczak, J. Pérez-Juste, P. Mulvaney, L. M. Liz-Marzán, *Chem. Soc. Rev.* **2008**, *37*, 1783–1791; c) S. E. Lohse, C. J. Murphy, *Chem. Mater.* **2013**, *25*, 1250–1261; d) C. B. Murray, C. R. Kagan, M. G. Bawendi, *Annu. Rev. Mater. Sci.* **2000**, *30*, 545–610; e) Y. Xia, Y. Xiong, B. Lim, S. E. Skrabalak, *Angew. Chem. Int. Ed.* **2009**, *48*, 60–103.

[2] a) A. P. Alivisatos, *J. Phys. Chem.* **1996**, *100*, 13226–13239; b) N. A. Beckers, S. Huynh, X. Zhang, E. J. Luber, J. M. Buriak, *ACS Catal.* **2012**, *2*, 1524–1534; c) N. A. Dehm, X. Zhang, J. M. Buriak, *Inorg. Chem.* **2010**, *49*, 2706–2714; d) S. Eustis, M. A. El-Sayed, *Chem. Soc. Rev.* **2006**, *35*, 209–217; e) K. L. Kelly, E. Coronado, L. L. Zhao, G. C. Schatz, *J. Phys. Chem. B* **2002**, *107*, 668–677; f) B. Luk'yanchuk, N. I. Zheludev, S. A. Maier, N. J. Halas, P. Nordlander, H. Giessen, C. T. Chong, *Nat. Mater.* **2010**, *9*, 707–715; g) E. J. McLaurin, M. S. Fataftah, D. R. Gamelin, *Chem. Comm.* **2013**, *49*, 39–41.

[3] a) E. C. Dreaden, M. A. El-Sayed, *Acc. Chem. Res.* **2012**, *45*, 1854–1865; b) D. A. Giljohann, D. S. Seferos, W. L. Daniel,

M. D. Massich, P. C. Patel, C. A. Mirkin, *Angew. Chem. Int. Ed.* **2010**, *49*, 3280–3294; c) S. Linic, P. Christopher, D. B. Ingram, *Nat. Mater.* **2011**, *10*, 911–921; d) J. Sun, D. K. Zhong, D. R. Gamelin, *Energ. Environ. Sci.* **2010**, *3*, 1252–1261; e) D. V. Talapin, J.-S. Lee, M. V. Kovalenko, E. V. Shevchenko, *Chem. Rev.* **2009**, *110*, 389–458; f) D. K. Zhong, D. R. Gamelin, *J. Am. Chem. Soc.* **2010**, *132*, 4202–4207.

[4] a) J. L. Walter, M. R. Jackson, C. T. Sims, *Alloying*, ASM International, Metals Park, Ohio, **1988**; b) P. Wilkes, *Solid State Theory in Metallurgy*, Cambridge University Press, New York, New York, **1973**; c) D. P. Woodruff, *The Chemical Physics of Solid Surfaces: Surface Alloys and Alloy Surfaces*, Vol. 10, Elsevier Science, Amsterdam, The Netherlands, **2002**.

[5] a) H. S. Choi, W. Liu, P. Misra, E. Tanaka, J. P. Zimmer, B. I. Ipe, M. G. Bawendi, J. V. Frangioni, *Nat. Biotechol.* **2007**, *25*, 1165–1170; b) B. R. Cuenya, *Thin Solid Films* **2010**, *518*, 3127–3150; c) M. Haruta, *Catal. Today* **1997**, *36*, 153–166; d) D. Kim, S. Park, J. H. Lee, Y. Y. Jeong, S. Jon, *J. Am. Chem. Soc.* **2007**, *129*, 7661–7665; e) M. Longmire, P. L. Choyke, H. Kobayashi, *Nanomedicine* **2008**, *3*, 703–717; f) Y. Zhang, X. Cui, F. Shi, Y. Deng, *Chem. Rev.* **2011**, *112*, 2467–2505.

[6] a) M. B. Cortie, A. M. McDonagh, *Chem. Rev.* **2011**, *111*, 3713–3735; b) R. Ferrando, J. Jellinek, R. L. Johnston, *Chem. Rev.* **2008**, *108*, 845–910; c) R. Ghosh Chaudhuri, S. Paria, *Chem. Rev.* **2011**, *112*, 2373–2433; d) M. Lattuada, T. A. Hatton, *Nano Today* **2011**, *6*, 286–308.

[7] a) C. Cui, L. Gan, M. Heggen, S. Rudi, P. Strasser, *Nat. Mater.* **2013**, *12*, 765–771; b) J. Greeley, M. Mavrikakis, *Nat. Mater.* **2004**, *3*, 810–815; c) J. Greeley, J. K. Nørskov, M. Mavrikakis, *Annu. Rev. Phys. Chem.* **2002**, *53*, 319–348; d) J. R. Kitchin, J. K. Norskov, M. A. Barteau, J. G. Chen, *J. Chem. Phys.* **2004**, *120*, 10240–10246.

[8] S. Sun, C. B. Murray, D. Weller, L. Folks, A. Moser, *Science* **2000**, *287*, 1989–1992.

[9] a) D. Ho, X. Sun, S. Sun, *Acc. Chem. Res.* **2011**, *44*, 875–882; b) F. Hu, H. M. Joshi, V. P. Dravid, T. J. Meade, *Nanoscale* **2010**, *2*, 1884–1891; c) H. B. Na, I. C. Song, T. Hyeon, *Adv. Mater.* **2009**, *21*, 2133–2148.

[10] M. G. Blaber, M. D. Arnold, M. J. Ford, *J. Phys.: Condens. Matter* **2010**, *22*, 143201.

[11] C. M. Andolina, A. C. Dewar, A. M. Smith, L. E. Marbella, M. J. Hartmann, J. E. Millstone, *J. Am. Chem. Soc.* **2013**, *135*, 5266–5269.

[12] a) P. Franke, D. Neuschütz, in *Binary Systems. Part 5: Binary Systems Supplement 1*, Vol. *19B5* (Eds.: P. Franke, D. Neuschütz), Springer Berlin Heidelberg, **2007**, pp. 1–4; b) H. Okamoto, T. B. Massalski, T. Nishizawa, M. Hasebe, *Bull. Alloy Phase Diagr.* **1985**, *6*, 449–454; c) H. Okamoto, T. B. Massalski, L. J. Swartzendruber, P. A. Beck, *Bull. Alloy Phase Diagr.* **1984**, *5*, 592–601.

[13] a) D. Bochicchio, R. Ferrando, *Phys. Rev. B* **2013**, *87*, 165435; b) A. U. Nilekar, A. V. Ruban, M. Mavrikakis, *Surf. Sci.* **2009**, *603*, 91–96.

[14] A. Christensen, P. Stoltze, J. K. Norskov, *J. Phys.: Condens. Matter* **1995**, *7*, 1047.

[15] a) J. F. Bondi, R. Misra, X. Ke, I. T. Sines, P. Schiffer, R. E. Schaak, *Chem. Mater.* **2010**, *22*, 3988–3994; b) Y. Vasquez, Z. Luo, R. E. Schaak, *J. Am. Chem. Soc.* **2008**, *130*, 11866–11867.

[16] J. Y. Park, E. S. Choi, M. J. Baek, G. H. Lee, S. Woo, Y. Chang, *Eur. J. Inorg. Chem.* **2009**, *2009*, 2477–2481.

[17] a) M. Brust, M. Walker, D. Bethell, D. J. Schiffrin, R. Whyman, *J. Chem. Soc., Chem. Comm.* **1994**, 801–802; b) T. Hyeon, *Chem. Comm.* **2003**, 927–934.

[18] W. M. Haynes, D. R. Lide, *CRC Handbook of Chemistry and Physics*, 92nd ed., CRC Press, Boca Raton, Fla., **2011**.

[19] V. K. LaMer, R. H. Dinegar, *J. Am. Chem. Soc.* **1950**, *72*, 4847–4854.

[20] a) C. J. DeSantis, A. C. Sue, M. M. Bower, S. E. Skrabalak, *ACS Nano* **2012**, *6*, 2617–2628; b) S. Zhou, G. S. Jackson, B. Eichhorn, *Adv. Func. Mater.* **2007**, *17*, 3099–3104.

[21] a) G. N. Glavee, K. J. Klabunde, C. M. Sorensen, G. C. Hadjipanayis, *Langmuir* **1993**, *9*, 162–169; b) K. J. Klabunde, J. V. Stark, O. Koper, C. Mohs, A. Khaleel, G. Glavee, D. Zhang, C. M. Sorensen, G. C. Hadjipanayis, in *Nanophase Materials*, Vol. *260* (Eds.: G. Hadjipanayis, R. Siegel), Springer Netherlands, **1994**.

[22] Y. Vasquez, A. K. Sra, R. E. Schaak, *J. Am. Chem. Soc.* **2005**, *127*, 12504–12505.

[23] J. L. Rousset, F. J. Cadete Santos Aires, B. R. Sekhar, P. Mélinon, B. Prevel, M. Pellarin, *J. Phys. Chem. B* **2000**, *104*, 5430–5435.

[24] Z. Zsoldos, T. Hoffer, L. Guczi, *J. Phys. Chem.* **1991**, *95*, 798–801.

[25] D. F. Evans, *J. Chem. Soc.* **1959**, 2003–2005.

[26] M. R. Knecht, J. C. Garcia-Martinez, R. M. Crooks, *Chem. Mater.* **2006**, *18*, 5039–5044.

[27] B. J. Auten, B. P. Hahn, G. Vijayaraghavan, K. J. Stevenson, B. D. Chandler, *J. Phys. Chem. C* **2008**, *112*, 5365–5372.

[28] a) F. Hu, K. W. MacRenaris, E. A. Waters, T. Liang, E. A. Schultz-Sikma, A. L. Eckermann, T. J. Meade, *J. Phys. Chem. C* **2009**, *113*, 20855–20860; b) C. W. Jung, P. Jacobs, *Magn. Res. Imaging* **1995**, *13*, 661–674.

[29] a) G. Wang, R. Guo, G. Kalyuzhny, J.-P. Choi, R. W. Murray, *J. Phys. Chem. B* **2006**, *110*, 20282–20289; b) J. Zheng, C. Zhang, R. M. Dickson, *Phys. Rev. Lett.* **2004**, *93*, 077402; c) J. Zheng, C. Zhou, M. Yu, J. Liu, *Nanoscale* **2012**, *4*, 4073–4083.

[30] A. Christensen, A. Ruban, P. Stoltze, K. W. Jacobsen, H. L. Skriver, J. K. Nørskov, F. Besenbacher, *Phys. Rev. B* **1997**, *56*, 5822.

[31] O. Crespo, M. C. Gimeno, A. Laguna, C. Larraz, M. D. Villacampa, *Chem. Eur. J.* **2007**, *13*, 235–246.

[32] P. Hänninen, H. Härmä, *Lanthanide Luminescence: Photophysical, Analytical, and Biological Aspects,* (Ed: O. S. Wolfbeis), Springer **2011**.

[33] J. Zhang, P. D. Badger, S. J. Geib, S. Petoud, *Angew. Chem. Int. Ed.* **2005**, *44*, 2508–2512.

[34] L. S. Bouchard, M. S. Anwar, G. L. Liu, B. Hann, Z. H. Xie, J. W. Gray, X. Wang, A. Pines, F. F. Chen, *Proc. Natl. Acad. Sci.* **2009**, *106*, 4085–4089.

[35] R. B. Lauffer, *Chem. Rev.* **1987**, *87*, 901–927.

[36] G. J. Stanisz, E. E. Odrobina, J. Pun, M. Escaravage, S. J. Graham, M. J. Bronskill, R. M. Henkelman, *Magn. Res. Med.* **2005**, *54*, 507–512.

[37] P. J. Klemm, W. C. Floyd III, C. M. Andolina, J. M. J. Fréchet, K. N. Raymond, *Eur. J. Inorg. Chem.* **2012**, *2012*, 2108–2114.

[38] Y.-w. Jun, J.-w. Seo, J. Cheon, *Acc. Chem. Res.* **2008**, *41*, 179–189.

[39] H. Jaganathan, R. L. Gieseck, A. Ivanisevic, *J. Phys. Chem. C* **2010**, *114*, 22508–22513.

[40] (Eds: J. A. Disegi, R. L. Kennedy, R. Pilliar), *Cobalt-Base Alloys for Biomedical Applications*, ASTM International, **1999**.

[41] S. Comby, D. Imbert, A.-S. Chauvin, J.-C. G. Bünzli, *Inorg. Chem.* **2005**, *45*, 732–743.